Article

Synthesis of bulk hexagonal diamond

https://doi.org/10.1038/s41586-025-09343-x

Received: 16 November 2021

Accepted: 1 July 2025

Check for updates

Liuxiang Yang[1], Kah Chun Lau[2], Zhidan Zeng[1], Dongzhou Zhang[3], Hu Tang[1], Bingmin Yan[1], Guoliang Niu[1], Huiyang Gou[1], Yanping Yang[1], Wenge Yang[1]✉, Duan Luo[4]✉ & Ho-kwang Mao[1,5]✉

Hexagonal diamond (HD), with anticipated physical properties superior than the known cubic diamond, has been pursued relentlessly since its inception 60 years ago[1]. However, natural and synthetic HD has only been preserved as a highly disordered component in fragile, heterogeneous mixtures of other nanocarbon structures that precludes determination of bulk properties and identification of HD as a bona fide crystalline phase[2–4]. Here we report the synthesis, recovery and extensive characterization of bulk HD by compressing and heating high-quality graphite single crystals under controlled quasi-hydrostatic conditions. We demonstrate the successful synthesis of 100-μm-sized to mm-sized, highly ordered, bulk HD. We observed direct transformation of graphite $(10\bar{1}0)$ orientation to HD (0002) and graphite (0002) to HD $(10\bar{1}0)$. The bulk sample consists of threefold intergrowth of tightly knitted 100-nm-sized crystals, predominantly HD with trace imperfections of cubic diamond. The interlayer bonds in HD are shortened with respect to intralayer bonds to optimize the HD structure. Notably, the hardness of HD is only slightly higher than cubic diamond. We anticipate that purifying the precursor graphite carbon and fine-tuning the high pressure–temperature (P–T) synthesis conditions may lead to higher-quality HDs.

Diamond has unmatched hardness and other extreme properties and is considered an ideal material for applications ranging from superabrasives, heat sinks, biosensors and quantum computation to photonic devices[5,6]. These properties originate from its unique building blocks of sp^3 carbon, bonded to each other with 1.54 Å bond length and 109.5° bond angle that form perfect tetrahedrons. This single type of bonding extends infinitely in two dimensions to form buckled honeycomb carbon layers and the layers stack with the same 1.54 Å bond in the third dimension to form the (111) planes of cubic diamond crystals. Such structure, however, also has a weakness. The (111) linkages are relatively weak between layers, resulting in weak (111) cleavage planes that limit the strength of diamond. Selectively shortening and strengthening interlayer bonds relative to the intralayer bonds would lower the symmetry of cubic diamond to hexagonal.

HD was predicted six decades ago[1] and subsequently synthesized by dynamic explosion[2] and static compression[3]. Natural HD was reported in the Canyon Diablo iron meteorite and named lonsdaleite after pioneer woman crystallographer Kathleen Lonsdale[7]. Although HD was theoretically predicted to have mechanical properties superior to cubic diamond[8], all previously known synthetic or natural HD samples are fragile, fine-grain mixtures of HD mixed with various proportions of cubic diamonds, amorphous carbon or residual graphite[4,7–12]. Hardness and other physical, chemical properties of HD could not be delineated from such a mixture of several phases.

Decades of relentless searching for pure, bulk HD has not led to a successful sample. Using the newly developed synchrotron beamline for dynamic shock experimentation, the formation mechanism of HD has been investigated by in situ X-ray diffraction (XRD) probe during shock compression[13–16], but the shocked sample was not recoverable for detailed analysis. By contrast, in-depth electron microscopy investigations on the Canyon Diablo meteorite and synthetic carbon samples revealed a large variety of complex nanostructures, but bulk HD beyond several atomic layers were never found, leaving even the existence of HD as a real phase in doubt[17–19].

These recent studies, however, disclosed highly valuable information for synthesizing pure HD and pointed out the potential solution. The large temporal and spatial stress–strain variations during the transient states of meteoritic impact is the main cause for the large variety of carbon nanostructures. As just one of the nanostructures, the formation of HD must be very sensitive and stringent to the local stress condition. Therefore, the pursuit of a macroscopic-size, pure HD sample would require a well-characterized single-crystal graphite precursor and follow its crystallographic change under uniform P–T conditions throughout the transition to the final recovered product. Distinguishing the recovered HD from other competing nanostructures would require a set of complementary macroscopic and microscopic diagnostic probes that, in combination, are capable of unequivocally and redundantly identify the product as a bulk HD sample.

Here we report comprehensive high P–T studies to establish the existence of HD as a bona fide phase, to determine its structure relation with its parental graphite, to synthesize bulk HD and to measure its optical and mechanical properties. Both a diamond anvil cell (DAC) and a multi-anvil press were used for compressing and heating single-crystal hexagonal graphite starting material under quasi-hydrostatic high-P condition. The precursor–product crystallographic relationships were monitored in situ at high P during the graphite-to-HD conversion by XRD and microscopic observation. Bulk HD synthesized at high P–T were successfully recovered at ambient conditions for further

[1]Center for High Pressure Science and Technology Advanced Research, Beijing, People's Republic of China. [2]Department of Physics and Astronomy, California State University, Northridge, Northridge, CA, USA. [3]GSECARS, University of Chicago, Lemont, IL, USA. [4]State Key Laboratory of Ultrafast Optical Science and Technology, Xi'an Institute of Optics and Precision Mechanics, Chinese Academy of Sciences, Xi'an, People's Republic of China. [5]Shanghai Key Laboratory of Material Frontiers Research in Extreme Environments, Shanghai Advanced Research in Physical Sciences, Shanghai, People's Republic of China. ✉e-mail: yangwg@hpstar.ac.cn; luoduan@opt.ac.cn; maohk@hpstar.ac.cn

ex situ investigations using XRD, high-resolution transmission electron microscopy (HRTEM), X-ray Raman spectroscopy (XRS), electron energy loss spectroscopy (EELS), ultraviolet (UV) Raman spectroscopy and Vickers hardness measurements. We demonstrate that HD is indeed the hexagonal counterpart of cubic diamond, with shortened and strengthened bonding between buckled honeycomb layers. These findings open new exploration of HD as a potentially superior technological material.

High *P*–*T* synthesis with in situ XRD probe

We conducted 40 experiments in the past 8 years to investigate key issues of the graphite-to-HD transition. We studied the pressure-induced change of XRD of single-crystal graphite sample (0001 flake) in neon hydrostatic pressure-transmitting medium in a DAC to keep the samples intact before, during and after the transition and to preserve the crystallographic orientations of the products and their relationship to the original graphite crystals. Increasing pressures up to 13.2 GPa (Fig. 1a), XRD clearly shows the typical single-crystal hexagonal [0001] near-zone-axis pattern of graphite, with six sharp $(10\bar{1}0)$ XRD spots equally distributed 60° apart on the inner constant 2θ circle and six $(11\bar{2}0)$ XRD spots on the next outer (smaller d-spacing) constant 2θ circle, with azimuth angles exactly in between (30° from) two adjacent $(10\bar{1}0)$ spots. The calculated d-spacings of $(10\bar{1}0)$ remain exactly $\sqrt{3}$ times that of $(11\bar{2}0)$ over the range 0–13.2 GPa, reflecting the hexagonal honeycomb configuration of graphite.

Increasing pressures from 13.2 to 20.0 GPa (Fig. 1b and Extended Data Fig. 1), however, the two circles behave differently: the outer circle expands substantially (d-spacing decreases), whereas the inner circle slightly shrinks (d-spacing increases). In this pressure range, we witnessed the strong compression of the previous G $(10\bar{1}0)$ d-spacing from 2.118 Å to 2.061 Å but slight expansion of the G $(11\bar{2}0)$ from 1.221 Å to 1.223 Å, resulting in a ratio of 1.68 instead of 1.73 (= $\sqrt{3}$). The extreme deviation from the strict $\sqrt{3}$ rule clearly demonstrates that the sample is no longer graphite but has transformed to a high-pressure crystalline carbon phase. This sharp single-crystal-like XRD pattern can be explained by one of the two alternatives: either a cubic diamond (D) single-crystal [111] zone axis image with the conversion of G $(10\bar{1}0)$ → D (111), G $(11\bar{2}0)$ → D (220) or three HD single crystals $[10\bar{1}0]$ zone axis images with G $(10\bar{1}0)$ → HD (0002), G $(11\bar{2}0)$ → HD $(11\bar{2}0)$. The HD alternative requires intergrowth of three separate domains of $[10\bar{1}0]$ zone axis patterns with their c-axis lying flat, 120° apart on the perpendicular (radial) plane to the DAC axis. The correct answer of the two alternatives relies on XRD of the sample in the radial direction that is blocked by the sample gasket, thus requiring quenching and retrieving the sample from the DAC.

The 20.0 GPa phase is not quenchable by simply releasing pressure at ambient T; heating at high pressure is needed to stabilize this phase. After laser heating to 1,400 °C at 20.0 GPa, the sample was decompressed and retrieved at ambient conditions for free-standing XRD study without the DAC. The zone-axis XRD pattern of the recovered specimen with incident X-ray beam along the original graphite c-axis is shown in Fig. 1d, which is taken with the same axial geometry as Fig. 1b, shows the same sixfold XRD patterns and carries the same diamond or HD alternative interpretations. In other words, Fig. 1d is either a single crystal of D [111] or three single crystals of HD $[10\bar{1}0]$ zone axis image; the sharp-spot, single-crystal-like pattern provides a precise orientation matrix for distinguishing the two alternatives. We conducted single-crystal XRD on the free-standing specimen based on the diamond UB matrix and did not find corresponding diamond peaks, whereas based on the HD UB matrix, we found an exact match, thus rejecting the diamond and proving the HD alternative. For instance, the radial pattern in Fig. 1c, which was taken with the X-ray beam in the direction perpendicular to the original graphite c-axis, reveals the intense 2.175 Å peak that is the characteristic HD $(10\bar{1}0)$ d-spacing but does not exist in cubic diamond. A series of diffraction spots were observed and the corresponding d-values are listed in Extended Data Table 1. All peaks can be well indexed with the HD phase (SG $P6_3/mmc$, a = 2.52 Å, c = 4.16 Å)[11,12]. In conclusion, single-crystal XRD of the recovered specimen is predominantly crystalline HD, although we cannot rule out a minor component of cubic diamond escaping XRD at the several percent level.

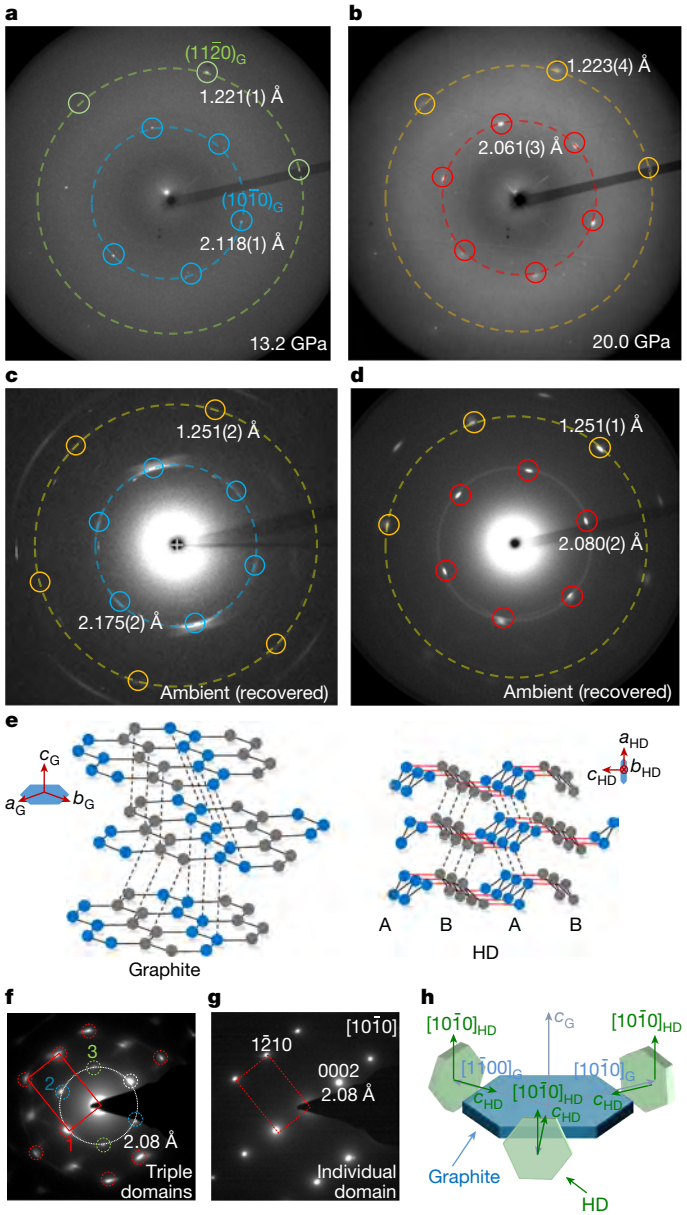

Fig. 1 | Single-crystal phase transition from graphite to HD under high pressure and high temperature and their epitaxial crystallographic relationship. a,**b**, Near-c-axis XRD pattern on graphite sample taken at 13.2 and 20.0 GPa. **c**,**d**, XRD patterns of recovered HD sample after laser heating to 1,400 °C at 20.0 GPa taken with incident X-ray perpendicular and parallel to the c-axis of the starting graphite sample. The diffraction spots in **a**, **b** and **d** all show a clear hexagonal symmetry. **e**, The atomic transformation from graphite to HD. Black solid and dashed lines connecting spheres of the same colours form new honeycombs of HD and red lines on the c-axis form bonds between HD honeycombs. Blue and black spheres represent the close-packed planes of HD in the ABAB stacking sequence. **f**, SAD pattern of the recovered specimen from a large area (1 μm in diameter) showing a hexagonal-like pattern, similar to the XRD result in **d**. **g**, SAD pattern from a 200-nm area showing a twofold symmetry that can be well indexed by HD $[10\bar{1}0]$ zone axis pattern of a single nanocrystal. **h**, Schematic of the epitaxial relationship between graphite and HD.

Our HD specimen transformed from a graphite single crystal under controlled quasi-hydrostatic *P*–*T* condition to the highly long-range-ordered, single-crystal-like HD is fundamentally distinctive from the disordered nanoprecipitation or dense planar defects in cubic diamond matrix found in shock-compressed natural meteorites or synthetic carbon samples[3,17–19]. With the advantage of following the crystallographic orientation of the single-crystal graphite through the transition to the recovered single-crystal-like HD, we can now unambiguously determine the crystallographic relation of single-crystal graphite and oriented polycrystalline HD as G (0001)//HD (10$\bar{1}$0), G (10$\bar{1}$0)// HD (0001) and G [$\bar{1}$2$\bar{1}$0]//HD [$\bar{1}$2$\bar{1}$0] (refs. 11,12) (Fig. 1e). Similar to the transformation mechanism proposed for the direct conversion of graphite to cubic diamond[20], the formation of HD is expected to proceed through an intermediate structure[21] (Fig. 1e). The growth of HD from the coherent interface involves the transition of the flat carbon honeycomb layer in graphite to the buckled carbon honeycomb layer of HD, which aligns parallel to the {10$\bar{1}$0} planes of the original graphite. Owing to the threefold degeneracy of the G {10$\bar{1}$0} class, the original single-crystal graphite must split into a polycrystalline aggregate of three sets of HD nanocrystals with HD (0002) corresponding to original G (10$\bar{1}$0), G (0$\bar{1}$10) and G ($\bar{1}$100). The orientations of all HD nanocrystals in each set are well aligned. Their *c*-axes are perfectly aligned within 1° in the original G (0002) plane and 120° ± 0.5° apart to give the sharp XRD spots as in the XRD patterns of three HD single crystals (Fig. 1d), whereas their *a*-axes may have rotational deviation around each *c*-axis by as much as ±5°, as shown by the arc spreading in Fig. 1c. The average grain size calculated from the HD (10$\bar{1}$0) peak width based on the Scherrer formula is 70 nm.

Atomistic characterization with HRTEM

We further examined the HD specimen at the atomic scale using HRTEM. A plane-view transmission electron microscopy (TEM) specimen was prepared by precise cutting of the recovered HD specimen in its original G (0001) orientation using focused ion beam (FIB) technology. The selected-area electron diffraction (SAD) pattern (Fig. 1f) from the specimen using a 1-μm-diameter aperture shows the ostensible sixfold symmetry with a *d*-value of 2.08 Å, consistent with the XRD image in Fig. 1d. When the aperture diameter decreases to about 200 nm, only a reduced number of diffraction spots corresponding to a twofold symmetry remains (Fig. 1g) and can be indexed as a HD [10$\bar{1}$0] zone axis pattern. The large and small SAD patterns (Fig. 1f,g) again independently rejected the cubic diamond [111] alternative and unequivocally demonstrated that the specimen consists of three sets of HD nanocrystalline domains with HD (0001) parallel to the three symmetric G (10$\bar{1}$0) of the original graphite single crystal (Fig. 1h). Diffraction contrast image analysis further confirms the triple-twinned HD microstructure with domain size around 100 nm (Extended Data Fig. 3), consistent with the XRD estimate of 70 nm based on peak width. It is worth noting that tilting of electron diffraction patterns also allow us to confirm the 3D crystallographic symmetry to distinguish HD from cubic diamond unequivocally. The tilt series of SAD patterns and HRTEM images from several major zone axes of one HD variant (Extended Data Figs. 4 and 5) confirm that the recovered sample is a submicron aggregate of bona fide HD.

The characteristic structural difference between diamond and HD is the ABC and AB stacking sequences of buckled carbon honeycomb layers, respectively. Therefore, the best way to distinguish them is to view the stacking sequence from the D [110] or the HD [2$\bar{1}\bar{1}$0] direction. Figure 2a is taken along HD [2$\bar{1}\bar{1}$0] direction, in which a large-area HD with pure AB stacking can be seen, which provides direct evidence of HD. Figure 2b shows the HRTEM image taken along the HD [0001] direction from a cross-sectional TEM sample. The carbon atoms in this direction are arranged in a honeycomb lattice, which indicates a hexagonal lattice configuration in HD similar to the basal plane of graphite.

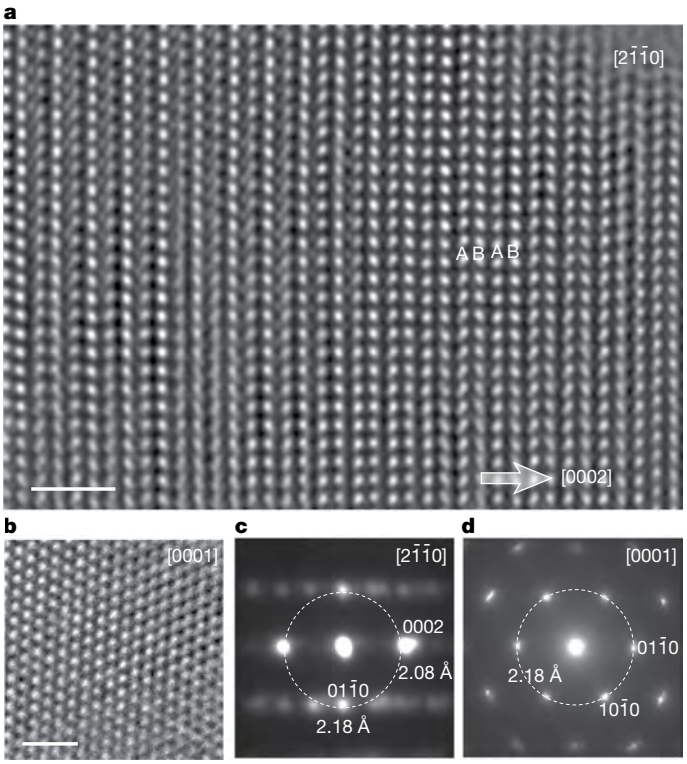

Fig. 2 | HRTEM images and corresponding SAD patterns of the bulk HD sample were acquired along different zone axes. a,**b**, HRTEM images along HD [2$\bar{1}\bar{1}$0] and [0001] zone axes showing a large area of HD with AB stacking and honeycomb configuration, respectively. Scale bars, 1 nm. **c**,**d**, SAD pattern along [2$\bar{1}\bar{1}$0] and [0001] using a 200-nm selected-area aperture. **c**, Extinction of (0001) diffraction owing to strict AB stacking. **d**, SAD along HD [0001] showing hexagonal diffraction spots with a *d*-value of 2.18 Å.

The SAD pattern (Fig. 2c) taken with a selected-area aperture (200 nm in diameter) shows the extinction of (0001) diffraction spots owing to strict AB stacking. The SAD pattern (Fig. 2d) taken along the HD [0001] direction shows hexagonal diffraction spots with a *d*-value of 2.18 Å, which has been carefully calibrated by the *d*-values of gold, distinguished from the D (111) *d*-spacing of 2.06 Å. In summary, TEM examination of our specimen shows monotonous intergrowth of well-oriented HD nanocrystals consistent with the XRD investigation. A small amount of cubic diamond is sometimes found as a (ABC) stacking defect in the nanocrystalline HD, but this is too small to be observable in the SAD pattern.

Bond length probe through Raman spectroscopy

Back to our original issue of HD shortening the bond length between the buckled honeycomb diamond layers, optical Raman spectroscopy provides valuable information on bond length, angles and strength that can also be used as fingerprints for phase identification. HD has a high luminescence background with optical visible excitations that often overwhelms the Raman signals. We overcame this challenge by using a 325-nm UV excitation laser[22] and obtained high-quality HD Raman spectra (Fig. 3a). Three peaks with vibration frequencies at 1,321, 1,529 and 1,249 cm^{-1} (in the order of peak intensity) have been observed. The absence of graphite G band at 1,583 cm^{-1} and D band at 1,370 cm^{-1} and the cubic diamond singular sharp band at 1,332 cm^{-1} (ref. 23) indicates the absence of graphite and cubic diamond. Our peaks are in good agreement with previous measurements of HD (ref. 22) but very different from theoretical simulation based on singular bond length HD structure that predicted three active Raman vibration modes at

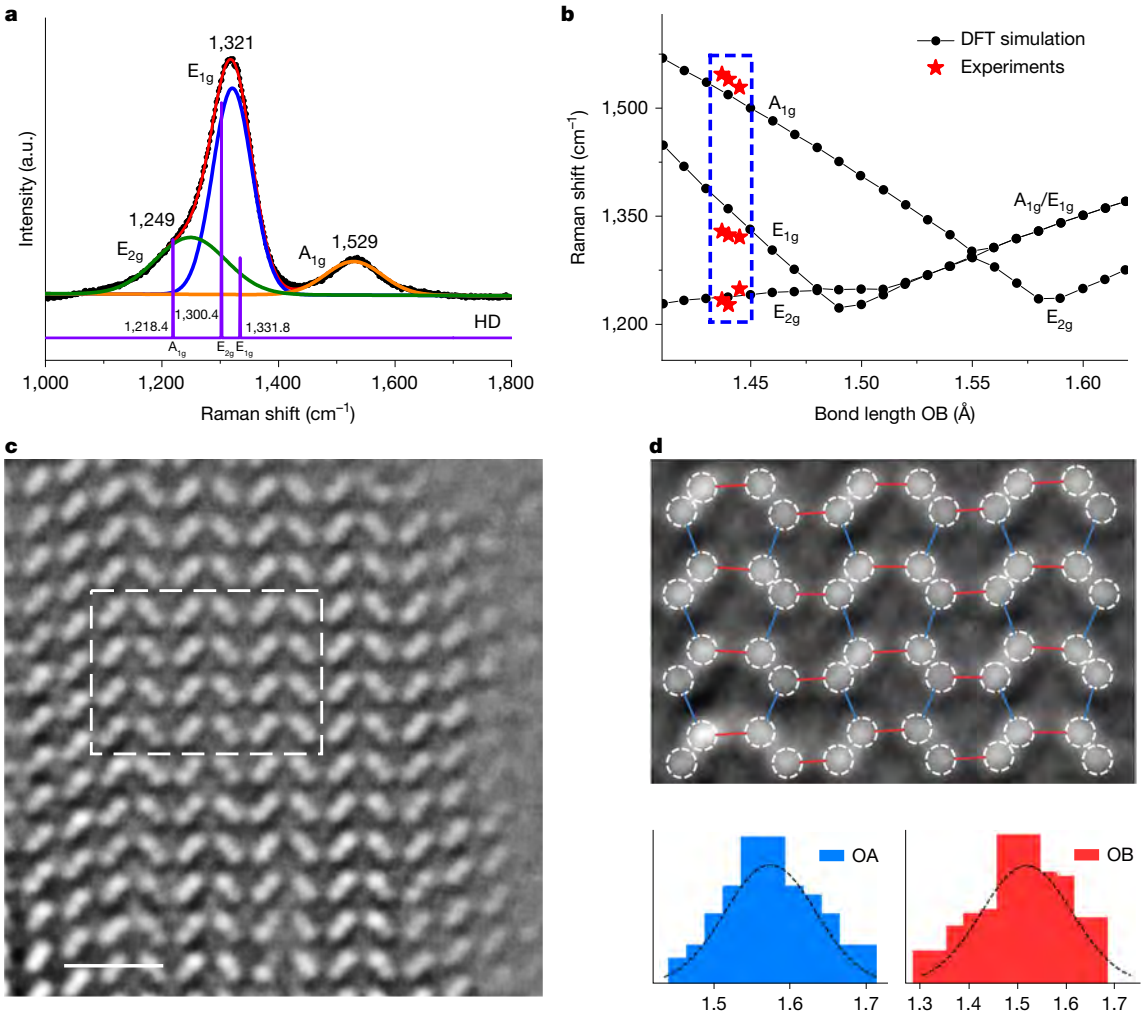

Fig. 3 | The two distinct bond lengths characteristic of HD were determined through complementary techniques: UV Raman spectroscopy, simulated Raman spectra and AC-HRTEM. a, UV Raman spectrum of the recovered HD sample showing three peaks (1,249, 1,321 and 1,529 cm^{-1}), marked by different colours. The bottom purple Raman spectrum is calculated on the basis of an ideal HD structure (ref. 24). **b**, Calculated Raman spectra of HD based on bond length OB shows three Raman modes (A_{1g}, E_{1g} and E_{2g}). Experimentally observed Raman vibration frequencies are indicated by red stars. **c**,**d**, AC-HRTEM image of a HD variant along [$2\bar{1}\bar{1}0$] ([100] in three Miller index) (**c**) and a statistical analysis on bond length from the dashed box (**d**) shows two distinguishable bond lengths on average: a longer one (blue) 1.58 ± 0.05 Å along the [0, 8, $\bar{8}$, $\bar{3}$] ([1, 2, $\bar{3}$/8] in three Miller index) direction and a shorter one (red) 1.50 ± 0.08 Å along the [0, 0, 0, 1] ([001] in three Miller index) direction. Scale bar, 0.5 nm. a.u., arbitrary units.

1,300.4, 1,331.8 and 1,218.4 cm^{-1} (refs. 24,25). The clear difference further substantiates that the carbon atomic arrangement in HD deviates from the singular bond length model.

Direct observation of two bond lengths

As for the optical Raman measurements, we typically focus the probing laser spot to 5–10 μm in diameter and the Raman signal represents the bulk average of the measured area. To confirm the presence of two bond lengths, we proceeded to atomic resolution and used aberration-corrected HRTEM (AC-HRTEM) in a very thin area (around 2 nm) to image atom arrangement in a unit cell directly. Figure 3c shows an AC-HRTEM image along the HD [$2\bar{1}\bar{1}0$] zone axis and the carbon dumbbells with a projected separation of 0.89 Å is clearly distinguished. Both bonds, OA (blue) and OB (red), lie in the plane perpendicular to [$2\bar{1}\bar{1}0$] and their bond lengths can be measured directly from the [$2\bar{1}\bar{1}0$] zone axis HRTEM image. In the enlarged HRTEM image, we found that bond length OB along the [0001] direction is shorter than OA along the HD [$\bar{1}2\bar{1}0$] direction. A statistical analysis on bond length and bond angle in a 0.8 × 1.2-nm^2 area confirms the two distinguishable bond lengths: a shorter one (red) 1.502 ± 0.079 Å along the [0001] direction and a longer one (blue) 1.578 ± 0.049 Å along the [0, 8, $\bar{8}$, $\bar{3}$] ([1, 2, $\bar{3}$/8] in three Miller index) direction (Fig. 3c, and Extended Data Fig. 6) and a relatively large distribution in bond angle of 112.1 ± 2.8° (Extended Data Fig. 6), which is similar to the nanodomain structure reported in ref. 26. Although the bond lengths exhibit a broad range, the presence of two distinct bond lengths in HD is well supported by statistical analysis. The tetrahedral symmetry of the sp^3-bonded carbon in HD is reduced to a distorted trigonal pyramid geometry with three OA bonds forming the buckled honeycomb layer and an OB bond linking two layers. Figure 3b shows our density functional theory (DFT) calculations (see the 'Simulations' section in Methods) of HD Raman vibration frequencies as a function of OB bond length. For OB at 1.44 Å, the three observed Raman peaks, 1,321, 1,529 and 1,249 cm^{-1} corresponding to E_{1g}, A_{1g} and E_{2g} Raman active modes, respectively, match well with the AC-HRTEM result in Fig. 3d. The A_{1g} Raman active mode corresponds to the stretching mode of OB = 1.44 Å, whereas E_{1g} and E_{2g} Raman active modes are attributed to the stretching mode of OA = 1.58 Å. As a bulk sample probe, optical Raman spectroscopic results are consistent with the OA/OB two-bond-length model and also indicate that the sample

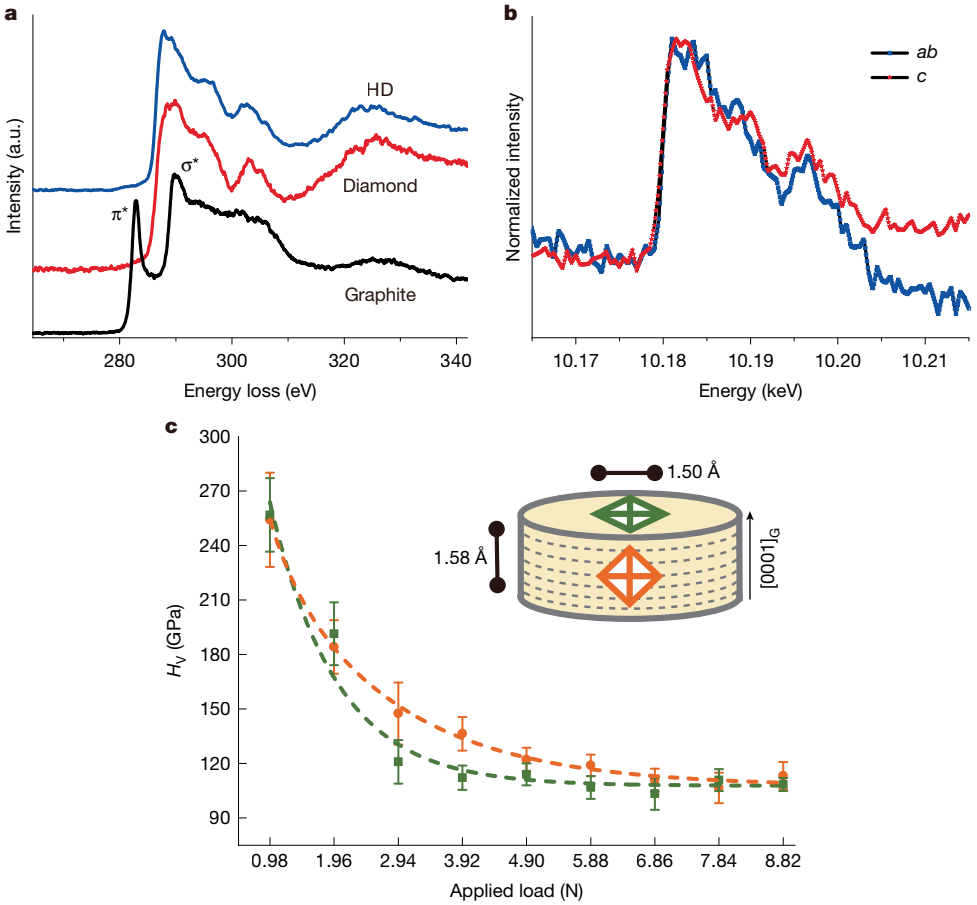

Fig. 4 | Pure sp³ bonding state and the excellent mechanical properties of bulk HD. a, EELS spectra of carbon k-edge from HD, diamond and graphite. **b**, X-ray Raman spectra on recovered HD samples with *ab* and *c* orientation. All results indicate 100% sp^3 bonding in the HD. **c**, Vickers hardness tests of HD along two directions with different load (N) up to 8.8 N. Inset, schematic of the hardness test positions on the sample and the C–C bond lengths in these two orientations are also labelled. The HD [10$\bar{1}$0] direction is parallel to the *c*-axis of the pristine graphite disk. Green symbols indicate indenting perpendicular to the HD *c*-axis. a.u., arbitrary units.

consists of only HD. Furthermore, we conducted a classic Rietveld analysis of the 'power diffraction pattern' from integrating XRD with as much orientation as possible from a recovered bulk HD sample, in which the two distinct bond lengths characteristic of the HD structure was confirmed (Extended Data Fig. 7).

Pure sp^3 confirmation with EELS and XRS

Graphite-to-diamond (or HD) transition is a change of carbon bonding from sp^2 π bonds to sp^3 σ bonds, which can be diagnosed by EELS or XRS. We conducted EELS measurements during our TEM studies of HD and observed complete transition to sp^3 σ bonds (Fig. 4a and Extended Data Figs. 8 and 9). However, EELS does not have penetration power and we conduct XRS, the energy loss spectroscopy using high-energy X-rays as the excitation source, to study the interior of the bulk sample[27]. No π bond contribution was detected (Fig. 4b), meaning that all of the graphite sp^2 π bonds have completely transformed to sp^3 σ bonds in the recovered HD sample.

Microhardness test on a large-volume press sample

With the confirmed synthesis of HD in the DAC, we proceeded to investigate the hardness of HD that required larger samples than DAC could produce. A 1-mm-diameter HD disk was synthesized from hexagonal graphite crystal at 20.0 GPa and 1,800 °C in a large-volume press. The details of sample preparation and hardness test are described in Methods. The Vickers hardness measurements in two orientations are illustrated in the inset of Fig. 4c. Up to the maximum load of 8.8 N, the Vickers hardness–load curves of measurements parallel and perpendicular to the *c*-axis of the original graphite reached the same value of 110 GPa, which are consistent with that of natural diamond (110 GPa) on the D (110) surface[28]. The bulk HD consists of intergrowth of 100-nm-sized crystallites with minor stacking defects of cubic diamonds. Because hardness is defined by the weakest component of the bulk specimen, the observed hardness of the bulk indicates that HD has hardness greater than or equal to cubic diamond. Further improvements to eliminate minor diamond components will give a definitive answer to the HD hardness.

In summary, with optimized pressure and temperature synthesis conditions, we have successfully synthesized a large, uniform HD sample from single-crystal graphite precursor. High-energy synchrotron XRD studies confirm that the bulk HD crystals follow a strict crystallographic orientation relationship to the original graphite crystal. The complete conversion of graphite sp^2 π bonds to HD sp^3 σ bonds is confirmed by XRS studies of the bulk sample with hard X-ray and by EELS studies at the atomic scale with electron microscopy. HRTEM and SAD studies confirm the same crystallographic orientation relationship as observed by XRD on the bulk sample and show the atomic-resolution, nominally homogeneous 2H stacking sequence in triple-twinned configuration with domain size around 100 nm. The UV Raman spectrum, HRTEM and DFT simulation all disclose the two-bond-length character of HD. Our results unambiguously demonstrate the existence of HD as a bona fide

phase of carbon with superior hardness like cubic diamond and has the optimal buckled honeycomb layered structure comprising distorted sp^3 tetrahedron units with regular 1.58 Å intralayer bond and shortened 1.50 Å interlayer bond that strengthens the linkage between layers relative to the cubic diamond structure. Notably, this is just the beginning; HD as a hexagonal variant of cubic diamond has been predicted with many extremely favourable mechanical, electrical, thermal and optical properties comparable with and complementary to diamond. HD presents great opportunities for exploration in the P–T conditions of synthesis, dopants in the precursor graphite and nanocrystallinity to optimize the desirable specific features and to engineer the ideal sp^3 carbon allotrope.

Online content

Any methods, additional references, Nature Portfolio reporting summaries, source data, extended data, supplementary information, acknowledgements, peer review information; details of author contributions and competing interests; and statements of data and code availability are available at https://doi.org/10.1038/s41586-025-09343-x.

1. Ergun, S. & Alexander, L. E. Crystalline forms of carbon: a possible hexagonal polymorph of diamond. *Nature* **195**, 765–767 (1962).
2. E. I. du Pont de Nemours and Company. Netherlands Patent Release No. 6506395 (22 November 1965).
3. Hanneman, R. E., Strong, H. M. & Bundy, F. P. Hexagonal diamonds in meteorites: implications. *Science* **155**, 995–997 (1967).
4. Shiell, T. B. et al. Nanocrystalline hexagonal diamond formed from glassy carbon. *Sci. Rep.* **6**, 37232 (2016).
5. Prawer, S. & Greentree, A. D. Diamond for quantum computing. *Science* **320**, 1601–1602 (2008).
6. Aharonovich, I., Greentree, A. D. & Prawer, S. Diamond photonics. *Nat. Photon.* **5**, 397–405 (2011).
7. Frondel, C. & Marvin, U. B. Lonsdaleite, a hexagonal polymorph of diamond. *Nature* **214**, 587–589 (1967).
8. Pan, Z., Sun, H., Zhang, Y. & Chen, C. Harder than diamond: superior indentation strength of wurtzite BN and lonsdaleite. *Phys. Rev. Lett.* **102**, 055503 (2009).
9. Kraus, D. et al. Nanosecond formation of diamond and lonsdaleite by shock compression of graphite. *Nat. Commun.* **7**, 10970 (2016).
10. Utsumi, W. & Yagi, T. Formation of hexagonal diamond by room temperature compression of graphite. *Proc. Jpn. Acad. B* **67**, 159–164 (1991).
11. Yagi, T., Utsumi, W., Yamakata, M., Kikegawa, T. & Shimomura, O. High-pressure *in situ* x-ray-diffraction study of the phase transformation from graphite to hexagonal diamond at room temperature. *Phys. Rev. B* **46**, 6031–6039 (1992).
12. Bundy, F. P. & Kasper, J. S. Hexagonal diamond—a new form of carbon. *J. Chem. Phys.* **46**, 3437–3446 (1967).
13. Stavrou, E. et al. Detonation-induced transformation of graphite to hexagonal diamond. *Phys. Rev. B* **102**, 104116 (2020).
14. Turneaure, S. J., Sharma, S. M., Volz, T. J., Winey, J. M. & Gupta, Y. M. Transformation of shock-compressed graphite to hexagonal diamond in nanoseconds. *Sci. Adv.* **3**, eaao3561 (2017).
15. Volz, T. J. & Gupta, Y. M. Elastic moduli of hexagonal diamond and cubic diamond formed under shock compression. *Phys. Rev. B* **103**, L100101 (2021).
16. Baek, W. et al. Unique nanomechanical properties of diamond–lonsdaleite biphases: combined experimental and theoretical consideration of Popigai impact diamonds. *Nano Lett.* **19**, 1570–1576 (2019).
17. Németh, P. et al. Lonsdaleite is faulted and twinned cubic diamond and does not exist as a discrete material. *Nat. Commun.* **5**, 5447 (2014).
18. Murri, M. et al. Quantifying hexagonal stacking in diamond. *Sci. Rep.* **9**, 10334 (2019).
19. Németh, P. et al. Complex nanostructures in diamond. *Nat. Mater.* **19**, 1126–1131 (2020).
20. Luo, K. et al. Coherent interfaces govern direct transformation from graphite to diamond. *Nature* **607**, 486–491 (2022).
21. Luo, D. et al. Atomistic evidence of nucleation mechanism for the direct graphite-to-diamond transformation. *Carbon* **229**, 119538 (2024).
22. Smith, D. C. & Godard, G. UV and VIS Raman spectra of natural lonsdaleites: towards a recognised standard. *Spectrochim. Acta A* **73**, 428–435 (2009).
23. Ferrari, A., Robertson, J., Reich, S. & Thomsen, C. Raman spectroscopy of graphite. *Philos. Trans. R. Soc. A* **362**, 2271–2288 (2004).
24. Cui, H.-J. et al. Diamond polytypes under high pressure: a first-principles study. *Comput. Mater. Sci.* **98**, 129–135 (2015).
25. Flores-Livas, J. A. et al. Raman activity of sp^3 carbon allotropes under pressure: a density functional theory study. *Phys. Rev. B* **85**, 155428 (2012).
26. Kanasaki, J., Inami, E., Tanimura, K., Ohnishi, H. & Nasu, K. Formation of sp^3-bonded carbon nanostructures by femtosecond laser excitation of graphite. *Phys. Rev. Lett.* **102**, 087402 (2009).
27. Mao, W. L. et al. Bonding changes in compressed superhard graphite. *Science* **302**, 425–427 (2003).
28. Huang, Q. et al. Nanotwinned diamond with unprecedented hardness and stability. *Nature* **510**, 250–253 (2014).

Methods

Importance and controversies of the bulk HD sample

Since the discovery of lonsdaleite using XRD half a century ago, the transformation path from graphite to HD and the crystal structure and microstructure of HD have been stimulating great interest. Especially in the past decade, two advanced technologies have been used to further characterize this phase in more detail, namely, high-resolution electron microscopy, including HRTEM and EELS, integrated with XRD and optical Raman spectroscopy and so on on the atomic-scale microstructures of ostensibly quenched HD samples at ambient conditions and time-resolved XRD measurement on the phase transition dynamics during the shock-wave high P–T impact process. Several groups have re-examined the microstructure of HD from various sources of meteorites and shock-compressed materials and found that these samples actually contain a wide variety of complex carbon nanostructures, except real HD. The observations of highly dense planar defects including stacking fault and twinning, intergrowth of atomic layer cubic diamond and graphite and no more than a few layers of HD present in other complex carbon phases lead to question of whether HD is a discrete material[17–19,29–31]. On the other hand, the recent developments in advanced synchrotron techniques allow scientists to observe the dynamic process during the phase transition in a shock-compression experiment. A series of research works at the Advanced Photon Source shows that a highly oriented pyrolytic graphite shock-compressed along the c-axis to 50 GPa transforms to highly oriented elastically strained HD with its $(10\bar{1}0)$ plane parallel to the graphite basal plane[13–16,32]. This certainly represents a notable scoring in support of shock-produced HD but still falls short of establishing HD as a bona fide bulk material because the only data were collected at high P–T shock conditions. Without the quenched sample and its TEM data, the validity is still subject to alternative interpretation as mixtures of these two polytype structures.

These recent works, however, have also revealed three very important tips. First, the highly stressful shock-wave impact processes produced by nature or in laboratories tend to generate a wide variety of complex carbon nanostructures but are unlikely to produce a uniform bulk HD. Such a high-stress process must be avoided in the quest for HD. Second, for understanding the transition mechanism, it is effective to monitor the crystallographic change using XRD the synthesis process from the precursor material through the transition to the final product. Third, the final HD product must be verified with the full suite of advanced microstructure diagnostic tools to confirm HD against other nanostructured carbon. Our study takes a new approach to synthesize bulk HD sample under hydrostatic P–T conditions, watch the epitaxial crystallographic evolution during compression with in situ single-crystal XRD measurement and recover it at ambient conditions for further stringent TEM, XRD and Raman diagnoses, thus providing a critical test for the controversy. Furthermore, we synthesized millimetre-sized bulk HD pure phase with a large-volume multi-anvil press for mechanical testing and confirmed its superhardness like that of cubic diamond, predicted from theoretical modelling but which has never been tested.

Sample preparation and synchrotron characterization

A high-quality HD has been synthesized under high pressure and temperature in a DAC. The pristine material is a 60 μm (diameter) × 20 μm (height) disk cut from a millimetre-sized single-crystal graphite by using a micro-laser drilling system[33]. Then, it was loaded into a 100-μm-diameter rhenium gasket chamber in a laser heating DAC. Pressure was monitored by the ruby fluorescence method. When the applied pressure was greater than 20.0 GPa, and the sample was heated to more than 1,400 °C with a YAG laser, the black graphite turned transparent. On cooling and decompression to ambient conditions, this transparent sample can be recovered.

In situ single-crystal XRD observation of the epitaxial crystallographic evolution under compression

Previously reported lonsdaleite samples from various sources of meteorites and shock-compressed processes show rather complex microstructure and mixture of multiphases. We deduced that differential stress during shock compression is the main cause for the formation of complex nanostructures. To minimize the environmental stress and intrinsic stress from polycrystalline graphite aggregate, we started the DAC experiment with a well-shaped single-crystal graphite sample in hydrostatic neon pressure medium. We were able to keep the starting graphite and final HD in single-crystal-like quality and monitor the crystal orientation evolution by synchrotron XRD during the compression, heating and transformation to HD.

As shown in Extended Data Fig. 1, at 13.2 GPa, the graphite $(\bar{1}100)$ and $(\bar{1}2\bar{1}0)$ peaks maintain good single-crystal diffraction sharpness and ratio of d-spacing at exact $\sqrt{3}$, which indicate that the sample is in the graphite phase. Before transferring to the HD phase at 20.0 GPa, we witnessed the emergence and growth of the epitaxial HD (0002) and $(\bar{2}110)$ peaks with consumption of graphite $(\bar{1}100)$ and $(\bar{1}2\bar{1}0)$ peaks. The new peaks with d-spacings 2.061 Å and 1.223 Å form completely at 20.0 GPa and the ratio of d-spacing clearly deviate from the strict $\sqrt{3}$ rule, meaning that graphite symmetry is broken.

On laser heating to 1,400 °C at 20.0 GPa, we were able to preserve the HD phase to ambient conditions. With the ostensible nature of single-crystal-like HD, we conducted XRD with the X-ray beam along and perpendicular to the c-axis of pristine graphite single crystal. The integrated XRD patterns show an outstanding and well-separated 2.175 Å peak, the characteristic diffraction from HD $(01\bar{1}0)$ d-spacing (Extended Data Fig. 2). Comparing a weak shoulder from previous reports[19] on the samples with dense planar defects, our most intense $(01\bar{1}0)$ peak indicates a well-preserved long-range ordering along the HD $(01\bar{1}0)$ crystallographic plane.

By rotating the recovered specimen, a series of diffraction spots was observed and the corresponding d-values are listed in Extended Data Table 1. Comparison with previous reports from Yagi et al.[11] and Bundy and Kasper[12] shows good consistency with their results.

TEM observation

To prepare the TEM sample, we first retrieved the HD from high P–T treatments and transferred the sample from the DAC chamber to a clean marble mortar with a tiny pin. Then, we crushed the recovered sample into powder by using the marble mortar and pestle. Finally, we dispersed the crushed powder onto a holey carbon grid. We also used the FIB technique to prepare plane-view and cross-sectional TEM specimens.

X-ray and UV Raman measurements

X-Ray Raman was performed with a silicon (555) analyser crystal aligned to receive the inelastic scattering intensity from the sample. The (555) Si crystal was set to reflect 10.175-keV X-rays and the incident beam energy was tuned from 10.165 keV to 10.215 keV with energy step size 0.1 eV. UV Raman experiments on the quenched samples from high P–T experiments were conducted using a Renishaw inVia Raman microscope with a 325-nm HeCd laser. This UV laser minimized the interference of fluorescence in Raman measurements. A low-power laser was used in the measurements to avoid any damage to the samples.

Simulations

To study the stability and vibration frequency of the proposed structure model, we carried out DFT calculations with plane-wave basis sets as implemented in the VASP code[34,35]. All calculations were spin-polarized and carried out by using the gradient-corrected exchange-correlation functional of Perdew, Burke and Ernzerhof under the projector augmented wave (PAW) method with plane-wave basis sets up to a kinetic

energy cut-off of 500 eV. The PAW method was used to represent the interaction between the core and valence electrons. The Kohn–Sham valence states (that is, 2s 2p for C) are expanded in plane-wave basis sets. For the geometry optimization calculations, the convergence criterion of the total energy was set to be within 1×10^{-6} eV of the gamma $8 \times 8 \times 8$ k-point grid and all of the atoms and geometries were optimized until the residual forces became less than 1×10^{-3} eV Å^{-1}. For the frequency calculations, the phonon values are obtained on the basis of density functional perturbation theory to compute the Hessian matrix. The Raman frequencies in Fig. 3b were obtained with separate DFT calculations with various OA and OB bond lengths while maintaining the hexagonal unit cell parameters and symmetry.

The molecular dynamics simulations were performed using a semi-empirical long-range carbon bond-order potential to model the interatomic interactions. The system simulated is an $8 \times 8 \times 8$ supercell of the unit cell and consists of 2,048 atoms. The anisotropic pressure is applied using a Nosé–Hoover barostat and the temperature is equilibrated using a Nosé–Hoover thermostat. All equilibration simulations were performed for at least 2 ns.

Microstructure of triple-twinned domains

The SAD pattern of the recovered specimen from a large area (1 μm in diameter) shows an ostensible sixfold symmetry with a *d*-value of 2.08 Å (Extended Data Fig. 3a). Extended Data Fig. 3b–d are convergent electron diffraction patterns from different sets of triple-twinned domains. Diffraction contrast image analysis further confirms the triple-twinned HD microstructure with domain size around 100 nm (Extended Data Fig. 3e). Dark-field images (Extended Data Fig. 3f–h) using diffraction spots 1, 2 and 3 marked in Extended Data Fig. 3a show the existence of three variants. HRTEM images across the interface of twinned domains and their fast Fourier transforms (FFTs) show clear single domain and intergrowth of twinned domains (Extended Data Fig. 3i–n).

Three-dimensional crystallographic symmetry with tilt series of electron diffraction and HRTEM

Tilt series of electron diffraction patterns allow us to confirm the crystallographic symmetry to distinguish HD from cubic diamond. As shown in Extended Data Fig. 4, we constructed the zone diffraction patterns and further confirmed that the phase is a HD from reciprocal space. Starting with sample along the $[10\bar{1}0]$ zone axis, tilting the sample 30° along (0002) results in the diffraction spots reaching the $[2\bar{1}\bar{1}0]$ zone axis. This is strong evidence for HD instead of cubic diamond. The HD $[10\bar{1}0]$ diffraction pattern alone can also be interpreted as either HD $[10\bar{1}0]$ or cubic diamond <112>, but the cubic diamond would reach a sixfold symmetry diffraction pattern by tilting either +19° or −19° along the $(1\bar{2}10)$ diffraction spot, which is ruled out in the present test.

In Extended Data Fig. 5, both real-space atomic-resolution HRTEM images (Extended Data Fig. 5a–c) and corresponding SAD patterns (Extended Data Fig. 5d–f) from three main zone axes [0001], $[2\bar{1}\bar{1}0]$ and $[10\bar{1}0]$ are presented and the simulated electron diffraction patterns (Extended Data Fig. 5g–i) show great agreement with the experimental observations.

Direct bond length detection from HRTEM image

Using the Laplacian of Gaussian blob detection algorithm implemented in the scikit-image package (https://scikit-image.org/docs/0.25.x/auto_examples/features_detection/plot_blob.html), we identified carbon atomic columns (Extended Data Fig. 6) from the HRTEM image presented in Fig. 3c. The *d*-spacings of the $(01\bar{1}0)$ plane and the (0002) plane were extracted to validate the calculation. The *d*-spacings of the $(01\bar{1}0)$ plane was found to be 2.175 ± 0.063 Å, averaged from the distances between 36 atom pairs. The *d*-spacing of the (0002) plane was found to be 2.080 ± 0.030 Å, averaged from the distances between 32 atom pairs. Both values agree very well with XRD measurements, which assures the accuracy of bond length measurement from the direct HRTEM. With that, the length of the longer (blue) bond was found to be 1.58 ± 0.05 Å, averaged from the distances between 18 atom pairs. The length of the shorter (red) bond was found to be 1.50 ± 0.08 Å, averaged from the distances between 20 atom pairs. The statistics show a clear difference in bond length along the $[0, 8, \bar{8}, \bar{3}]$ and [0001] directions.

The bond angles were also calculated in the same area. The bond angles were found to be 111.8 ± 2.9°, 112.3 ± 4.1°, 115.1 ± 2.1° and 109.1 ± 2.2°, respectively, for the angle between the red–green–yellow, green–yellow–blue, yellow–blue–red and blue–red–green atoms. The average bond angle is 112.1 ± 2.8°.

As per the above statistical analysis, the bond angle shows relatively large statistical errors (several degrees), but the bond length shows a good measurement uncertainty (less than 10 pm).

EELS to exclude diamond/graphite composite

EELS spectroscopy provides key information on the bond character to distinguish diamond (pure σ bond) and graphite (both σ and π bonds). Samples subjected for the EELS study are HD samples prepared by FIB, cubic diamond powders with average grain size of about 1 μm, crushed highly oriented pyrolytic graphite samples and glassy carbon without amorphous carbon. The default power-law profile was used for the background-subtraction model and we extend the background-subtraction window to 283 eV to reveal any intensity more clearly in the pre-edge region. Extended Data Fig. 6 shows carbon K-edge EELS spectra with/without background subtraction for HD and cubic diamond, to show the quality of the background subtraction. The EELS spectra are enlarged in the intensity axis to show the pre-edge structure indicated by the yellow arrows. There is a slightly noticeable pre-peak in the HD sample compared with the cubic diamond sample. Glassy carbon instead of highly oriented pyrolytic graphite is used as the standard to calculate the sp^2/sp^3 ratio using the method described in ref. 36. The estimated sp^2/sp^3 ratio is 3.04(±0.56)%. Because HRTEM images of our HD sample taken from different orientations and different areas with different focus conditions did not show a noticeable 0.33-nm graphitic lattice, we attribute the pre-peak (corresponding to about 3% sp^2/sp^3) to the surface amorphous carbon damaged from FIB TEM sample preparation.

Also, we estimated the EELS spectra of diamond/graphite composite by simply summing the EELS spectra of graphite (or amorphous carbon from holey carbon TEM grids) and diamond. Extended Data Fig. 9 shows these spectra using different percentages of graphite (or amorphous carbon). When the percentage is 1% (Extended Data Fig. 9), almost no noticeable pre-peak is observed. A small pre-peak becomes noticeable when the percentage is 3% (Extended Data Fig. 9). When the percentage is 5%, both pre-peaks are clearly noticeable. By overlaying the hex-diamond EELS (Extended Data Fig. 8a) on the sum spectra and EELS spectra in Extended Data Fig. 9, the estimated sp^2/sp^3 is around 3%.

In conclusion, EELS observations exclude the diamond/graphite composite model in our synthesized samples from the 20.0 GPa and 1,400 °C conditions.

Preparation and Vickers hardness measurements of large-size HD samples

Large-size samples (about 1 mm in diameter and approximately 70 μm in thickness) were synthesized with a high-pressure multi-anvil apparatus by applying 20.0 GPa pressure and 1,800 °C temperature for 20 min. The COMPRES 8/3 assembly used in experiments consists of $MgAl_2O_4$ + MgO octahedron (pressure medium), a rhenium heater and a $LaCrO_3$ thermal insulator. To reduce the deformation of samples during compression, the graphite disk was surrounded by cubic boron nitride powder. Pressure was calibrated at room temperature based on the phase transition of pressure-standard materials of GaAs (18.3 GPa) and GaP (23.0 GPa). Temperatures were monitored with a $W_{97}Re_3$-$W_{75}Re_{25}$

thermocouple. The recovered samples were checked by XRD to confirm the bulk HD phase. The hardness tests were conducted on the polished surfaces with a micro-Vickers hardness machine (FM-700, Future-Tech Corp.). Vickers hardness H_V was obtained by using different loads with a holding time of 10 s. H_V was determined from $H_V = 1{,}854.4F/L^2$, in which F (N) is the applied load and L (μm) is the arithmetic mean of the two diagonals of the Vickers indentation.

Data availability

The datasets for this study are available in the source data of the corresponding figures. Requests for more materials should be addressed to H.-k. Mao. Source data are provided with this paper.

29. Garvie, L. A. J., Németh, P. & Buseck, P. R. Transformation of graphite to diamond via a topotactic mechanism. *Am. Mineral.* **99**, 531–538 (2014).
30. Németh, P. et al. Diamond-graphene composite nanostructures. *Nano Lett.* **20**, 3611–3619 (2020).
31. Németh, P. et al. Diaphite-structured nanodiamonds with six- and twelve-fold symmetries. *Diam. Relat. Mater.* **119**, 108573 (2021).
32. Volz, T. J., Turneaure, S. J., Sharma, S. M. & Gupta, Y. M. Role of graphite crystal structure on the shock-induced formation of cubic and hexagonal diamond. *Phys. Rev. B* **101**, 224109 (2020).
33. Hrubiak, R., Sinogeikin, S., Rod, E. & Shen, G. The laser micro-machining system for diamond anvil cell experiments and general precision machining applications at the High Pressure Collaborative Access Team. *Rev. Sci. Instrum.* **86**, 072202 (2015).
34. Kresse, G. & Furthmüller, J. Efficient iterative schemes for ab initio total-energy calculations using a plane-wave basis set. *Phys. Rev. B* **54**, 11169–11186 (1996).
35. Kresse, G. & Furthmüller, J. Efficiency of ab-initio total energy calculations for metals and semiconductors using a plane-wave basis set. *Comput. Mater. Sci.* **6**, 15–50 (1996).
36. Wan, L. & Egerton, R. F. Preparation and characterization of carbon nitride thin films. *Thin Solid Films* **279**, 34–42 (1996).

Acknowledgements We are thankful for the financial support from the National Natural Science Foundation of China under grant no. U1930401, the National Science Fund for Distinguished Young Scholars (grant no. T2225027), Shanghai Science and Technology Committee, China (no. 22JC1410300) and Shanghai Key Laboratory of Material Frontiers Research in Extreme Environments, China (no. 22dz2260800).

Author contributions L.Y., Z.Z., D.Z. and W.Y. carried out the synchrotron experiment. D.L. performed the TEM characterization. L.Y. and W.Y. performed the experimental data analysis. K.C.L. performed the Raman spectrum calculation. H.T., B.Y., G.N. and H.G. performed the multi-anvil synthesis and Vickers hardness measurements. Y.Y. prepared the TEM sample by FIB. L.Y. and K.C.L. carried out DFT simulations. L.Y., W.Y. and H.-k.M. wrote the manuscript. H.-k.M. conceived and designed the project. All authors contributed to the discussion of the results and revision of the manuscript.

Competing interests The authors declare no competing interests.

Additional information

Correspondence and requests for materials should be addressed to Wenge Yang, Duan Luo or Ho-kwang Mao.

Peer review information *Nature* thanks Péter Nèmeth and the other, anonymous, reviewer(s) for their contribution to the peer review of this work.

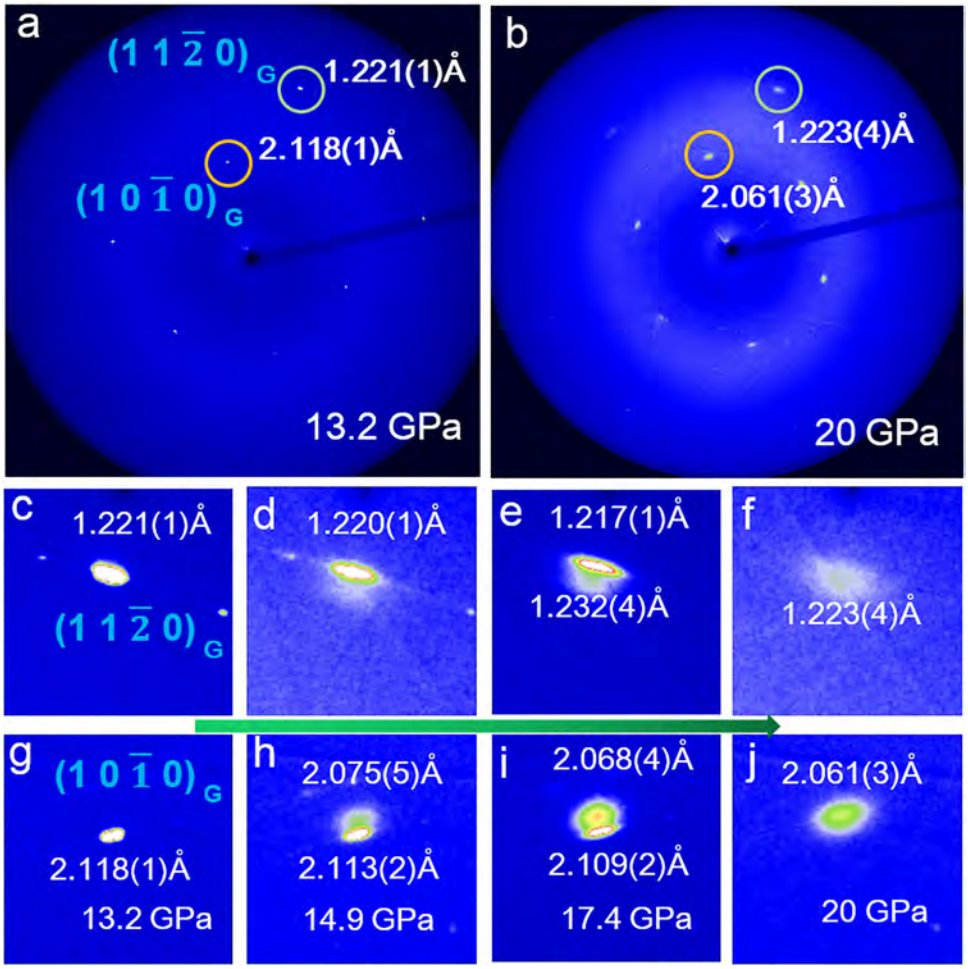

Extended Data Fig. 1 | XRD images of hexagonal graphite at different pressures before and after transition. a, 13.2 GPa. **b**, 20.0 GPa. The incident X-ray beam is parallel to the *c*-axis of pristine graphite. The graphite (10$\bar{1}$0) and (11$\bar{2}$0) diffraction spots at 13.2 GPa and the corresponding spots appearing at 20.0 GPa are labelled by orange and green circles in **a** and **b**, respectively. **c**–**j**, Evolution of the (11$\bar{2}$0) and (10$\bar{1}$0) diffraction spots under pressures between 13.2 GPa and 20.0 GPa. A fuzzy peak epitaxy to the graphite (10$\bar{1}$0) peak with a smaller *d*-spacing appears and grows at the expense of graphite (10$\bar{1}$0) from 14.9 GPa, whereas a similar evolution can be seen from the graphite (11$\bar{2}$0) peak but with a larger *d*-spacing from 17.4 GPa. At 20.0 GPa, both graphite (10$\bar{1}$0) and (11$\bar{2}$0) peaks disappear and the new peaks with *d*-spacings of 2.061 Å and 1.223 Å form completely.

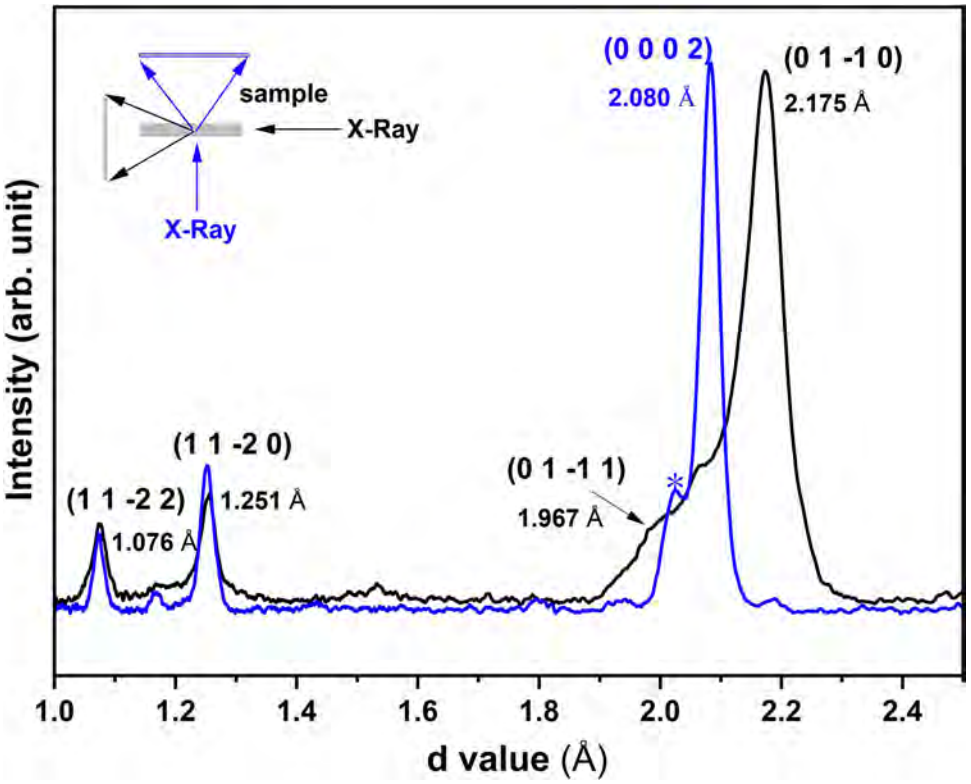

Extended Data Fig. 2 | The integrated XRD patterns from the recovered HD sample with incident X-ray beam along (blue) and perpendicular to (black) the *c*-axis of starting graphite crystal. The weak diffraction ring marked with * is from the glue for fixing the sample on the holder. In these two patterns, 2.175 Å and 2.080 Å diffraction peaks have the most intensity and separate well, which can be assigned to HD (01$\bar{1}$0) and (0002) diffraction peaks unequivocally.

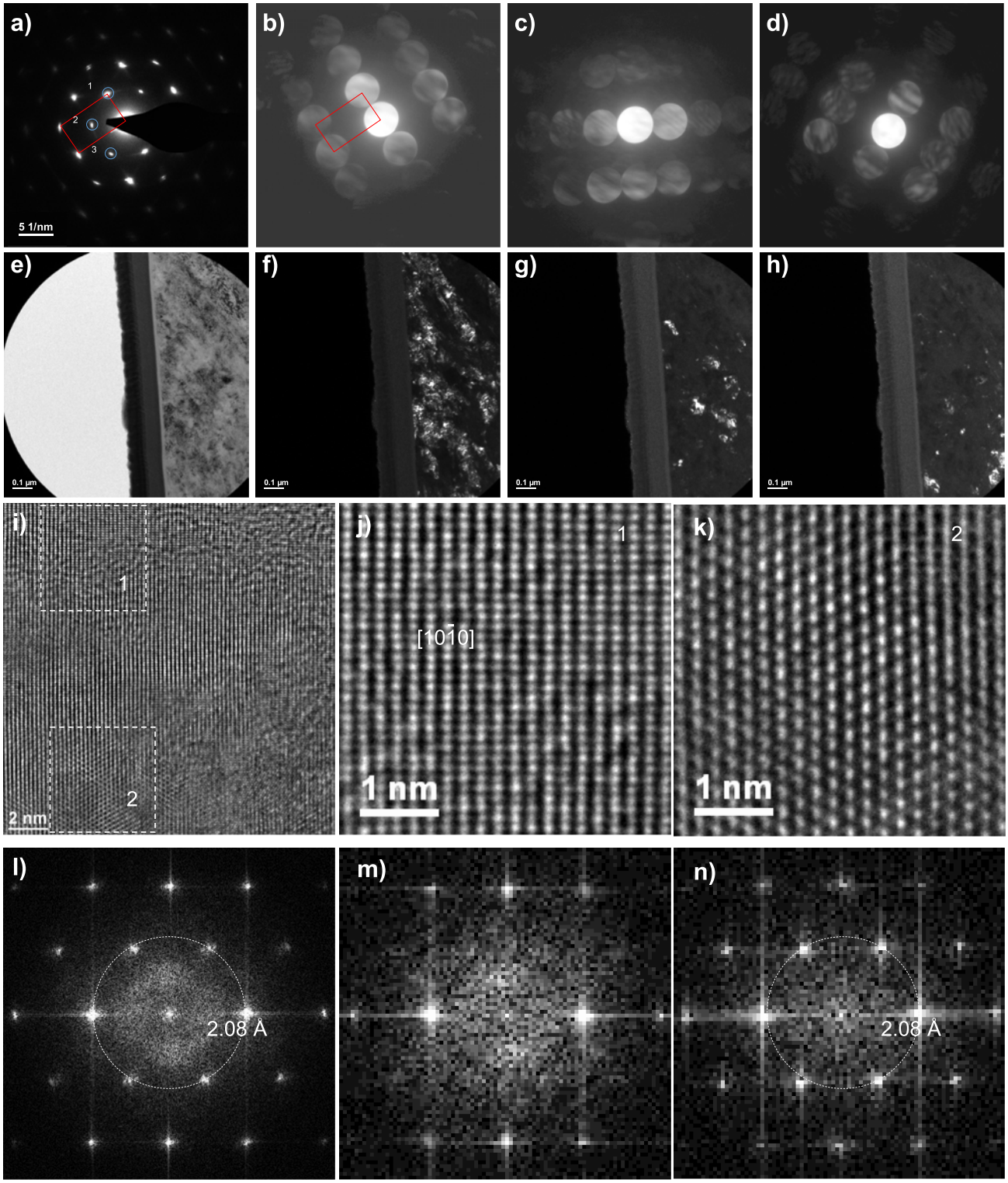

Extended Data Fig. 3 | TEM study of the microstructure in triple twinned HD domains. a, SAD pattern using a large, selected-area aperture. **b**–**d**, Convergent electron diffraction patterns showing three sets of diffraction patterns from each set of triple-twinned domain. Each variant has a twofold [10$\bar{1}$0] diffraction pattern separated by 120°. **e**, Bright-field TEM image showing triple-twinned microstructure in our high *P*–*T* synthesized HD. **f**–**h**, Dark-field images using diffraction spots 1, 2 and 3 marked in **a** show that there exist three variants. HRTEM images across the interface of twinned domains. **i**, A large-area HRTEM image encompassing all three twin domains. The corresponding FFT pattern (**l**) exhibits pseudo-hexagonal symmetry with a lattice spacing of 2.08 Å, consistent with the XRD data shown in Fig. 1d. **j**, An HRTEM image of a single domain (area 1) along the [10$\bar{1}$0] zone axis. The corresponding FFT pattern (**m**) reveals orthorhombic symmetry. **k**, An HRTEM image of the overlapping region of three twinned domains (area 2), showing pseudo-hexagonal symmetry with a lattice spacing of 2.08 Å, as shown in the FFT pattern (**n**).

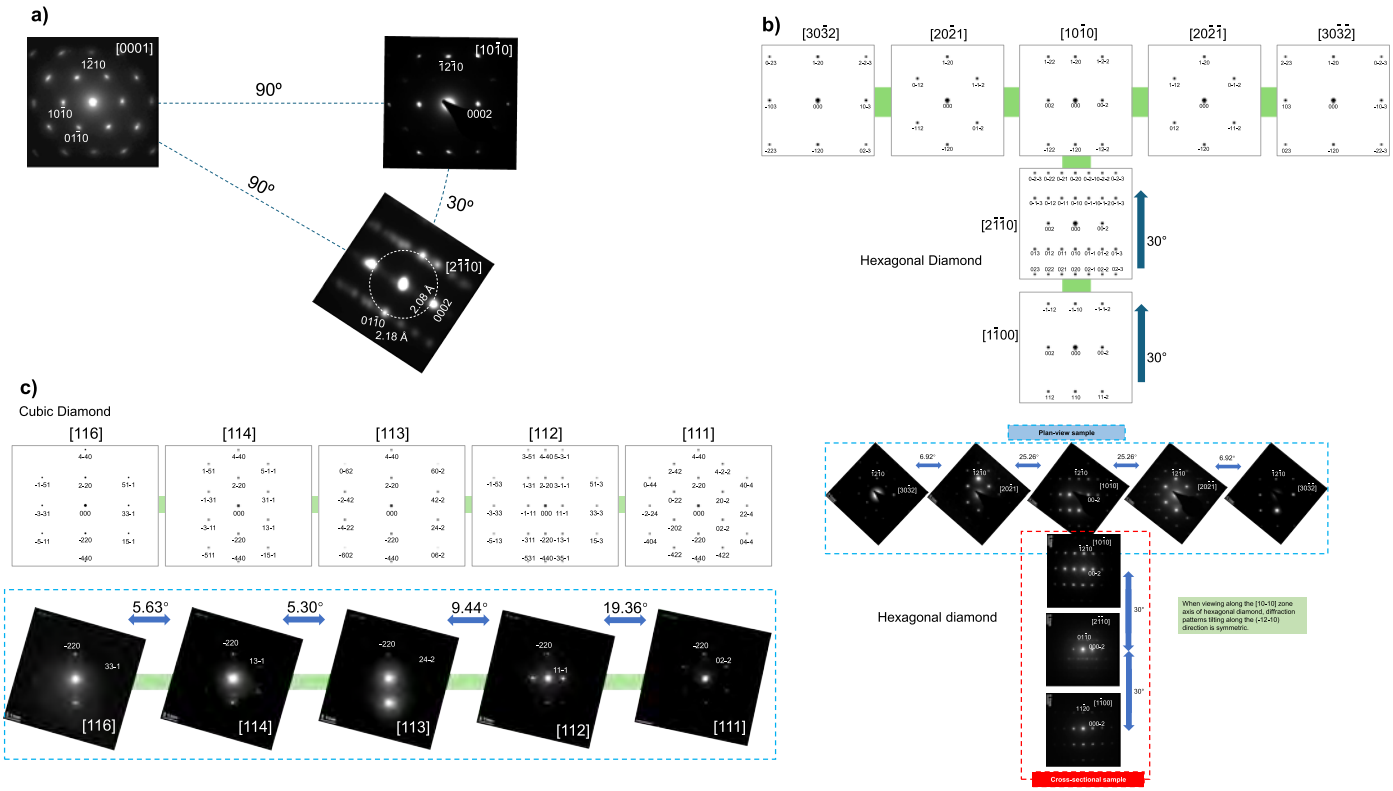

Extended Data Fig. 4 | Tilt series of electron diffraction patterns from hexagonal and cubic diamond domains. a, When sample is along the [10$\bar{1}$0] zone axis of HD, tilting the sample 30° along (0002) causes the diffraction spots to reach the [2$\bar{1}\bar{1}$0] zone axis, indicating in-plane sixfold symmetry. The [0001] zone axis diffraction was taken from a differently oriented grain. **b**,**c**, The simulated and experimental tilt series SAD patterns from hexagonal and cubic diamond samples. The precise matching in three-dimensional tilting SAD patterns confirm the crystallographic symmetry of HD. Tilt angles measured from experiments, as shown in the figure, match those from simulated diffraction patterns.

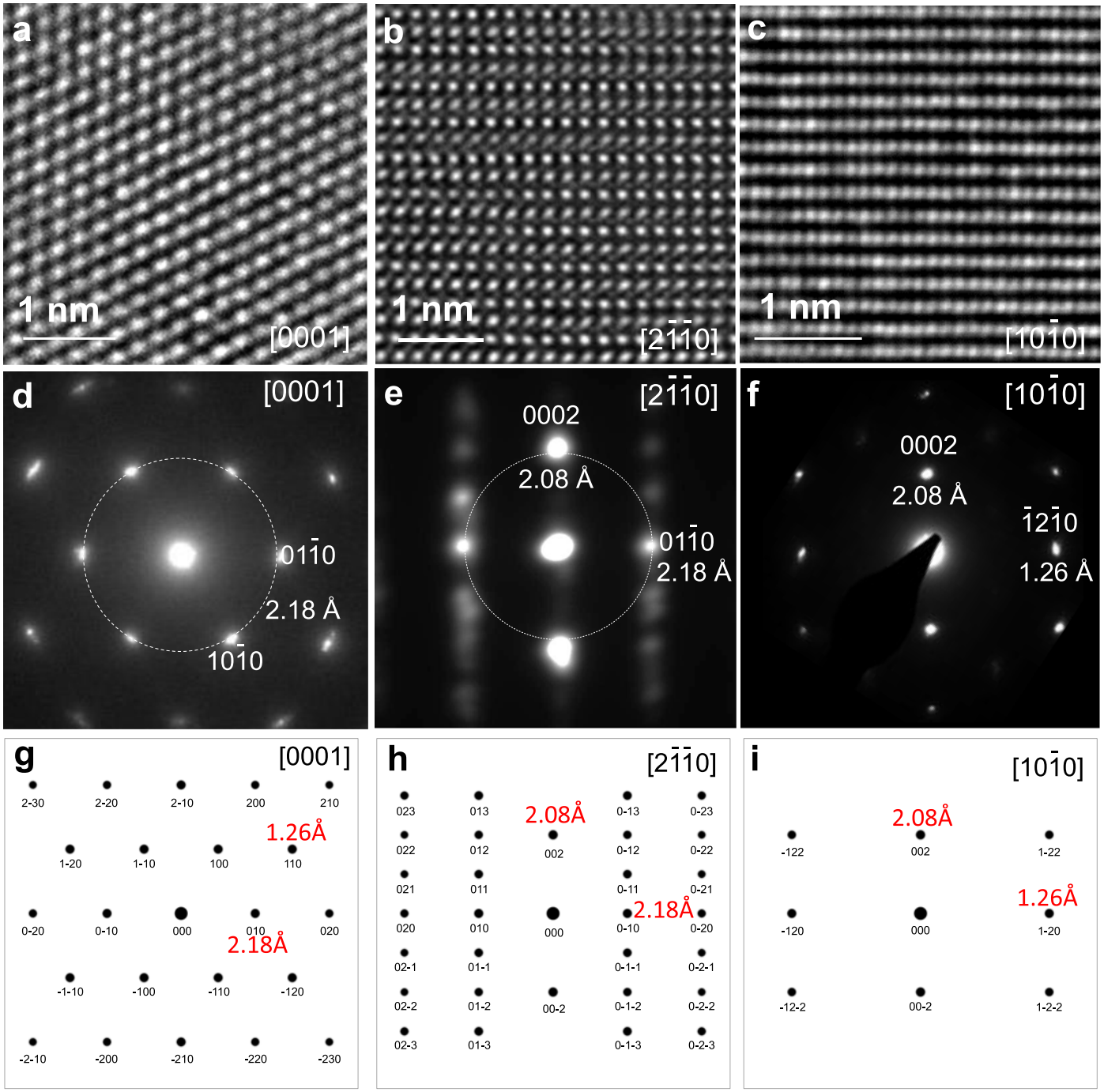

Extended Data Fig. 5 | HRTEM and electron diffraction patterns of HD from three major zone axes. a–i, HRTEM images (**a–c**), corresponding SAD patterns (**d–f**) and simulated electron diffraction patterns (**g–i**) from three main zone axes [0001], [2$\bar{1}\bar{1}$0] and [10$\bar{1}$0], respectively.

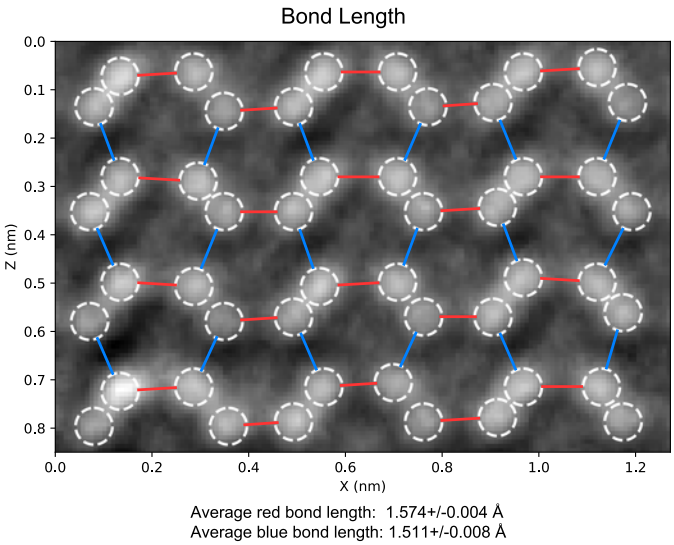

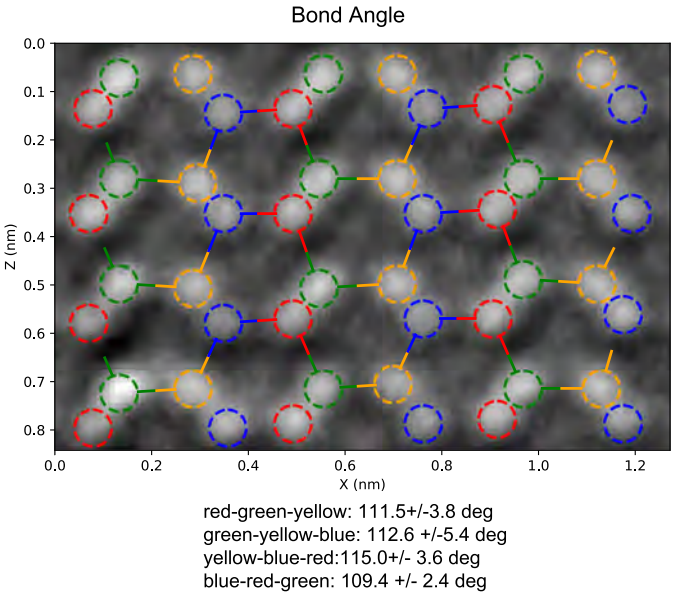

Extended Data Fig. 6 | Statistical analysis of bond length and bond angle from the HRTEM along the [$2\bar{1}\bar{1}0$] zone axis. A shorter (red) bond length 1.50 ± 0.08 Å along the (0001) direction and a longer (blue) bond length 1.58 ± 0.05 Å along the [0, 8, $\bar{8}$, $\bar{3}$] direction was retrieved from 20 pairs and 18 pairs C–C distance, respectively, using the Laplacian of Gaussian blob detection algorithm implemented in the scikit-image package. A relatively larger bond angle distribution with an average of 112.1 ± 2.8° was obtained. To verify the accuracy of atomic position identification, the *d*-spacing values of the ($01\bar{1}0$) and (0001) planes (labelled with yellow dashed lines) were analysed to be 2.175 ± 0.063 Å and 2.080 ± 0.030 Å, averaged from the distances between 36 and 32 atom pairs, respectively, which match the *d*-spacing values from XRD measurement very well.

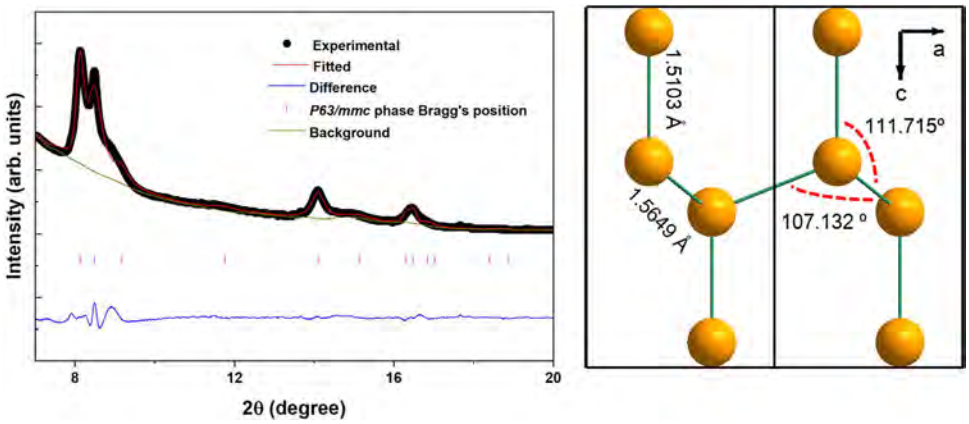

Extended Data Fig. 7 | Rietveld refinement on the integrated XRD pattern from a recovered HD sample with lattice constants $a = b = 2.5182$ Å and $c = 4.1780$ Å. The right panel presents the atom arrangement with two sets of bond length (1.5103 Å and 1.5649 Å) and two sets of bond angle (107.132° and 111.715°).

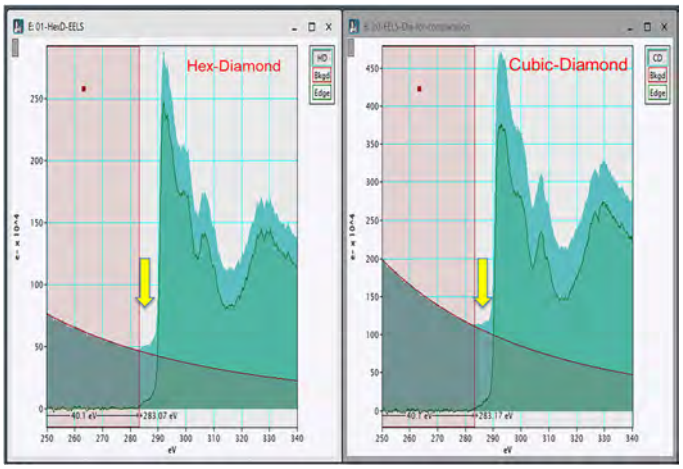

Extended Data Fig. 8 | EELS spectra from HD and cubic diamond. A very small pre-peak indicated by the yellow arrow in the HD EELS spectra can be seen. The estimated sp^2/sp^3 is around 3%, resulting from the amorphous surface layer owing to FIB sample preparation.

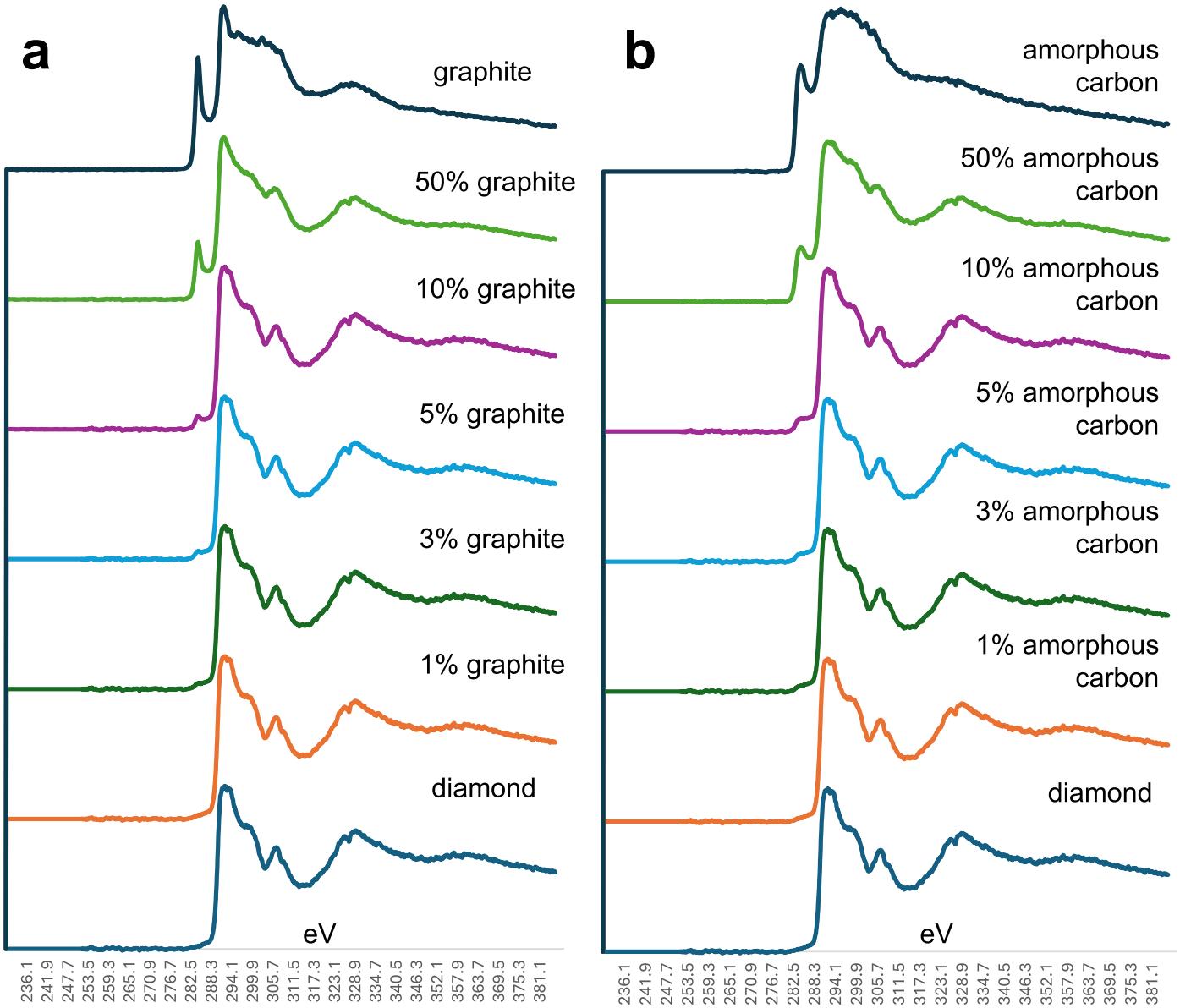

Extended Data Fig. 9 | EELS spectra from the mixture of different polytypes of carbon. a, EELS spectra summed from diamond and graphite with different percentages. **b**, EELS spectra summed from diamond and amorphous carbon with different percentages. All spectra are normalized with the maximum peak before the summation.

Extended Data Table 1 | Comparison of lattice constants with previous reports from Yagi et al.[11] and Bundy and Kasper[12]

Hexagonal diamond	Bundy (1967)	Yagi (1992)	Our results (observed)	Calculated (Å)
$01\bar{1}0$	2.19	2.180	2.175	2.184
0002	2.06	2.086	2.080	2.083
$01\bar{1}1$	1.92		1.967	1.934
$01\bar{1}2$	1.50		1.500	1.507
$11\bar{2}0$	1.26	1.256	1.251	1.261
$01\bar{1}3$	1.17		1.170	1.171
$02\bar{2}0$			1.085	1.092
$11\bar{2}2$	1.075	1.074	1.076	1.078
$P6_3/mmc$	a = 2.52 Å c = 4.12 Å	a = 2.513(6) Å c = 4.171(5) Å	a = 2.52 Å c = 4.16 Å	